

## Numerical Study of Singularity Formation in Relativistic Euler Flows

Pierre A. Gremaud<sup>1</sup> and Yi Sun<sup>2,\*</sup>

<sup>1</sup> *Department of Mathematics, North Carolina State University, Raleigh, NC, 27695, USA.*

<sup>2</sup> *Department of Mathematics, University of South Carolina, Columbia, SC 29208, USA.*

Received 22 December 2012; Accepted (in revised version) 30 January 2014

Communicated by Jan S. Hesthaven

Available online 17 April 2014

---

**Abstract.** The formation of singularities in relativistic flows is not well understood. Smooth solutions to the relativistic Euler equations are known to have a finite life-span; the possible breakdown mechanisms are shock formation, violation of the sub-luminal conditions and mass concentration. We propose a new hybrid Glimm/central-upwind scheme for relativistic flows. The scheme is used to numerically investigate, for a family of problems, which of the above mechanisms is involved.

**AMS subject classifications:** 35L67, 65M08, 65M25, 76Y05, 83C05, 83C75

**Key words:** Relativistic Euler equations, singularity formation, Glimm scheme, central-upwind scheme, hybrid method.

---

### 1 Introduction

Relativistic hydrodynamics plays a fundamental role in many fields of physics from astrophysics and cosmology to nuclear physics [3, 38]. The relativistic Euler equations considered in this paper describe the dynamics of a compressible perfect fluid in the context of special relativity, i.e., the fluid evolves in a flat Minkowski spacetime. These equations are valid away from large matter concentrations and in small regions of spacetime. They can be regarded as an approximation to the Euler-Einstein equations.

Elementary nonlinear waves for the relativistic Euler equations have been analyzed [1, 25, 35, 36]. Existence of entropy solutions for problems without vacuum state [33] as well as for problems with possible vacuum formation [22] has been established. The

---

\*Corresponding author. *Email addresses:* gremaud@ncsu.edu (P. A. Gremaud), yisun@math.sc.edu (Y. Sun)

mechanism by which singularities form is, however, not fully understood. While Pan and Smoller [29] has shown finite time singularity formation of any smooth solutions of the relativistic Euler equations for a perfect fluid, see Section 2, the *type* of singularity which occurs is unknown.

We present here a numerical investigation of singularity formation for solutions of the relativistic Euler equations both in two and three spatial dimensions with radially, respectively spherically, symmetric smooth initial data. We review existing numerical methods for relativistic hydrodynamics in Section 3. In order to numerically characterize the mechanisms by which singularities form, we propose a hybrid approach that combines standard finite difference methods in the smooth part of the flow with Glimm scheme near discontinuities and sharp gradients. The detection of sharp gradient areas is discussed in Section 3; details about the Riemann solver for the Glimm scheme are discussed in the Appendix.

The character of the numerical solutions is analyzed in a post-processing step. Naive ideas such as checking directly whether the Rankine-Hugoniot jump condition [23,32,37] holds at discontinuities are highly impractical because of the difficulties in evaluating all involved quantities. Instead, we use a detailed study of the numerical characteristic curves which is described in Section 4, along with our numerical results. For a family of problems in (2+1) dimensional spacetime with radial symmetry and (3+1) dimensional spacetime with spherical symmetry, we show that singularities occur through shock formation.

## 2 Basic equations and mathematical analysis

The relativistic Euler equations for a perfect fluid can be written as [29,33]

$$\partial_t \left( \frac{\rho c^2 + p}{c^2 - |v|^2} - \frac{p}{c^2} \right) + \nabla_x \cdot \left( \frac{\rho c^2 + p}{c^2 - |v|^2} v \right) = 0, \tag{2.1}$$

$$\partial_t \left( \frac{\rho c^2 + p}{c^2 - |v|^2} v \right) + \nabla_x \cdot \left( \frac{\rho c^2 + p}{c^2 - |v|^2} v \otimes v \right) + \nabla_x p = 0, \tag{2.2}$$

where  $\rho$  is the mass-energy density,  $p$  the pressure,  $c$  the speed of light. The vector  $v$  is defined as

$$v = \frac{cu}{\sqrt{1+|u|^2}},$$

where  $u$  is the velocity of the fluid. In  $d$  space dimensions ( $d=2$  or  $3$ ),  $u$ ,  $v$  and the space coordinates  $x$  are  $d$ -vectors. Hereafter, for convenience, we refer to  $v$  as the velocity. The system (2.1)-(2.2) is closed by an equation of state which we take as the  $\gamma$ -law:

$$p(\rho) = \sigma^2 \rho^\gamma, \quad \gamma \geq 1. \tag{2.3}$$

Further, a subluminal condition is assumed, i.e.

$$0 < p'(\rho) < c^2, \quad \text{for } \rho \in (\rho_1, \rho_2), \tag{2.4}$$

where  $0 \leq \rho_1 < \rho_2$ . For the isothermal case  $\gamma = 1$ , the above condition boils down to  $\sigma < c$ ; for  $\gamma > 1$ , we have  $p'(\rho_2) = c^2$  [29]. In our study, we take  $\gamma = 4/3$  and consider the Cauchy problem for (2.1)-(2.3) with initial data

$$\rho(x,0) = \rho_0(x), \quad v(x,0) = v_0(x) \quad (2.5)$$

for the unknowns  $\rho$  and  $v$ . The specific problems treated below correspond to localized in space perturbations from the quiescent state  $\rho = \bar{\rho}$  and  $v = 0$ , for some constant  $\bar{\rho} > 0$ . More precisely,  $\rho_0$  and  $v_0$  satisfy the following condition

$$(\rho_0(x) - \bar{\rho}, v_0(x)) = 0, \quad \text{for } |x| \geq R, \quad (2.6)$$

where  $R > 0$ , and  $\bar{\rho} > 0$  satisfies  $0 < p'(\bar{\rho}) < c^2$ .

Using the initial data of  $\rho_0$ ,  $v_0$  and  $R$  defined in (2.5) and (2.6), we define the characteristic pressure  $\bar{p}$ , speed  $\bar{v}$ , and time  $\bar{t}$  by

$$\bar{p} := p(\bar{\rho}), \quad \bar{v} := \max_{|x| \leq R} |v_0|, \quad \bar{t} := \frac{R}{\bar{v}}.$$

These quantities in turn can be used to define dimensionless dependent variables:  $v^* := \frac{v}{\bar{v}}$ ,  $\rho^* := \frac{\rho}{\bar{\rho}}$ ,  $t^* := \frac{t}{\bar{t}}$ ,  $\dots$ . Rewritten in terms of the non-dimensional variables, the system (2.1)-(2.3) takes the form (for the sake of concision, the "stars" are omitted)

$$\partial_t \hat{\rho} + \nabla_x \cdot (\tilde{\rho} v) = 0, \quad (2.7)$$

$$\partial_t (\tilde{\rho} v) + \nabla_x \cdot (\tilde{\rho} v \otimes v) + \nabla_x \left( \frac{1}{\gamma M^2} \rho^\gamma \right) = 0, \quad (2.8)$$

where, following [29], we have introduced

$$\tilde{\rho} = \frac{\rho + \frac{1}{\gamma} \frac{\beta^2}{M^2} \rho^\gamma}{1 - \beta^2 |v|^2}, \quad \hat{\rho} = \tilde{\rho} - \frac{\beta^2}{\gamma M^2} \rho^\gamma. \quad (2.9)$$

The two dimensionless parameters  $\beta$  and  $M$  are defined by

$$\beta := \frac{\bar{v}}{c}, \quad M := \frac{\bar{v}}{s} = \text{Mach number},$$

where  $s = \sqrt{p'(\bar{\rho})} = \sqrt{\sigma^2 \gamma \bar{\rho}^{\gamma-1}}$  is the sound speed in this non-dimensional setting. Note that in the limit  $c \rightarrow \infty$  ( $\beta \rightarrow 0$ ), we have  $\hat{\rho} \rightarrow \rho$  and  $\tilde{\rho} \rightarrow \rho$ , and the above system (2.7)-(2.8) reduces to the classical Euler equations.

To get more insight into the structure of the solutions, we consider a radially symmetric smooth initial data for the system (2.7)-(2.8) in  $(d+1)$ -dimensional spacetime,  $d = 2, 3$ . The resulting system is

$$\partial_t \hat{\rho} + \partial_r (\tilde{\rho} v_r) + \frac{d-1}{r} \tilde{\rho} v_r = 0, \quad (2.10)$$

$$\partial_t (\tilde{\rho} v_r) + \partial_r \left( \tilde{\rho} v_r^2 + \frac{1}{\gamma M^2} \rho^\gamma \right) + \frac{d-1}{r} \tilde{\rho} v_r^2 = 0, \quad (2.11)$$

where  $r = |x|$  is the distance from the origin, and  $v_r$  is the velocity in the radial direction.

In [29], Pan and Smoller prove that, given compactly supported non-trivial initial data, singularity formation of smooth solutions of the relativistic Euler equations in three space dimensions occurs in finite time. A similar result holds in two space dimensions.

**Theorem 2.1.** *Assume  $d = 2$  and*

$$\beta < M/\sqrt{2}. \tag{2.12}$$

*If, additionally, the initial conditions (2.5) satisfy*

$$\hat{\rho}_0 \geq 1, \tag{2.13}$$

$$v_0 \cdot x \geq 0, \tag{2.14}$$

$$\int \tilde{\rho}_0 v_0 \cdot x dx > \frac{3\pi/M}{1 - 2\frac{\beta^2}{M^2}} \left(1 + \frac{1}{\gamma}\right) \max \hat{\rho}_0. \tag{2.15}$$

*where (2.13) and (2.14) hold on domains of positive measure, then the smooth solutions of the Cauchy problem (2.5), (2.10)-(2.11) has a finite lifespan.*

*Proof.* The proof can be obtained by trivially adapting the proof of Theorem 3.2 and Remark 7 of [29] to the two-dimensional setting.  $\square$

In three space dimensions, i.e.,  $d = 3$ , conditions (2.12) and (2.15) are replaced by

$$\beta < M/\sqrt{3}, \tag{2.16}$$

$$\int \tilde{\rho}_0 v_0 \cdot x dx > \frac{16\pi/M}{3\left(1 - 3\frac{\beta^2}{M^2}\right)} \left(1 + \frac{1}{\gamma}\right) \max \hat{\rho}_0, \tag{2.17}$$

see Theorem 3.2, [29].

It is an open problem to predict what *type of singularities* are described by the above results. As noted in Remark 4 of [29], the possibilities are: a) shock formation, b) violation of the subluminal condition, c) mass concentration; see also Remark 5 of that paper. For the one-dimensional isothermal case, i.e.,  $p(\rho) = \sigma^2 \rho$ , Smoller and Temple [33] proved that for solutions with bounded variation that avoid the vacuum state, the subluminal condition guarantees the genuine nonlinearity of the system. Therefore, in that case, singularities must be shocks by Lax's theory [21]. In the more general setting considered here, our numerical results also predict shock formation to be the mechanism by which singularities form.

### 3 Numerical methods

In Newtonian fluid dynamics,  $\rho = \tilde{\rho} = \hat{\rho}$ , see (2.9), and consequently the conserved variables (i.e., the elements of the state vector,  $\rho$  and  $\rho v$ ) and the primitive variables  $\rho$  and  $v$

are related in a simple way. This can be confirmed by a cursory look at (2.7)-(2.8) where, ignoring the “hats and tildes”, one can easily compute the fluxes (quantities under the space derivatives) from the knowledge of the conserved variables (quantities under the time derivatives). This is not the case for relativistic hydrodynamics where the relationships between conserved and primitive variables are considerably more involved, see again (2.9). As a result, at each time step we need to solve a system of non-linear equations at every grid point to determine the primitive variables  $\rho$  and  $v$  from the conserved quantities; subsequently, the flux terms at that point are computed. In the present work, we use a variation of Newton’s method as non-linear solver. The computational cost is thus considerably higher for the numerical solution of relativistic problems than for their Newtonian counterparts.

Many Finite Difference (FD) methods developed in Newtonian fluid dynamics have been extended to relativistic hydrodynamics: Eulderink [11] explicitly derived a relativistic Roe’s Riemann solver [30]; Schneider et al. [31] carried out the extension of Harten, Lax, van Leer, and Einfeldt’s (HLLC) method [10, 15]; Martí and Müller [26] extended the piecewise parabolic method (PPM) of Woodward and Colella [7]; Dolezal and Wong [9] put into practice ENO techniques; Yang et al. [41] developed a kinetic beam scheme for relativistic gas dynamics; Zhang and MacFadyen [44] applied the adaptive mesh refinement techniques to relativistic hydrodynamics; recently Tang et al. applied several techniques into relativistic hydrodynamics, such as adaptive moving mesh methods, direct Eulerian GRP schemes, and Runge-Kutta discontinuous Galerkin methods with WENO limiters [16, 42, 43, 45]. High-order central schemes have also successfully been applied to the relativistic hydrodynamics equations, see, e.g., [2, 8, 24]. We refer the reader to the review articles [12, 27] as well as [3, 40] and the references therein for more numerical methods and simulation results of numerical relativistic hydrodynamics.

By construction, FD methods contain a certain amount of numerical viscosity which has the positive effect of selecting the correct entropy solution. Unfortunately, this also induces loss of sharpness in the solution near steep gradients. In order to numerically identify shock formation, it is essential that discontinuities are not spread through numerical dissipation. Glimm’s random choice algorithm, see [13] and/or Appendix, sharply resolves discontinuities and is thus a natural choice. It has been employed for relativistic hydrodynamics [4, 39]. As the method is only formally first order accurate, we limit the use of Glimm’s scheme to those regions of the fluid where steep gradients are present. Away from these locations, a FD scheme is applied. A hybrid approach based on Glimm’s scheme and Lax-Friedrichs and Lax-Wendroff schemes was for instance taken in [39]; similar methods have been advocated in other fields as well [17, 28, 46]. We propose here a hybrid method based on Glimm’s scheme and a second order accurate central-upwind scheme [20] in the regions where the fluid flow is sufficiently smooth. In addition, a fractional step method is taken to handle the source terms. Central schemes for conservation laws have recently attracted a lot of attention due to their simplicity, efficiency and robustness. These schemes are based on an exact evolution of an approximate piecewise polynomial reconstruction, do not require any (approximate) Riemann problem solvers,

and can be therefore used as black-box solvers for a variety of problems [18–20].

For the resolution of (2.10)-(2.11), we use here a second-order piecewise linear min-mod reconstruction to approximate the spatial derivatives and a second-order Runge-Kutta scheme to advance in time. The method is (formally) globally second-order accurate. Numerical boundary conditions at the origin are imposed

$$\rho\left(-\frac{\Delta r}{2}\right) = \rho\left(\frac{\Delta r}{2}\right), \quad v_r\left(-\frac{\Delta r}{2}\right) = -v_r\left(\frac{\Delta r}{2}\right),$$

where  $\Delta r$  is the mesh size. The detection of discontinuities (or sharp gradients) is an important part of the design of the hybrid method. The goal is to prevent smearing of large gradients due to the central-upwind scheme while at the same time avoiding the overuse of the Riemann solver in the Glimm scheme in smooth regions. As observed in [39], robust detection algorithms can be based on relative changes of physical quantities at neighboring states. Here, we compute

$$\theta_i = |\rho_i - \rho_{i-1}| / (\rho_i + \rho_{i-1}),$$

and locally apply the Glimm scheme if  $\theta_i > 0.05$ . This criterion was experimentally determined and represents a good balance between optimal shock resolution and overall global accuracy, i.e., minimum smearing of rarefaction waves.

To illustrate the hybrid approach, we solve the one-dimensional radial relativistic Euler equations (2.10)-(2.11) with both the central-upwind scheme and our hybrid method along the radial direction. For comparison, we also include the full two-dimensional solution to (2.7)-(2.8) computed by the two-dimensional central-upwind scheme. The initial conditions are described in Fig. 1 and correspond to globally  $C^1$ , piecewise polynomial, compactly supported perturbations of the quiescent state  $\rho = \bar{\rho}$  with  $\bar{\rho} = 1$ , see again (2.6).

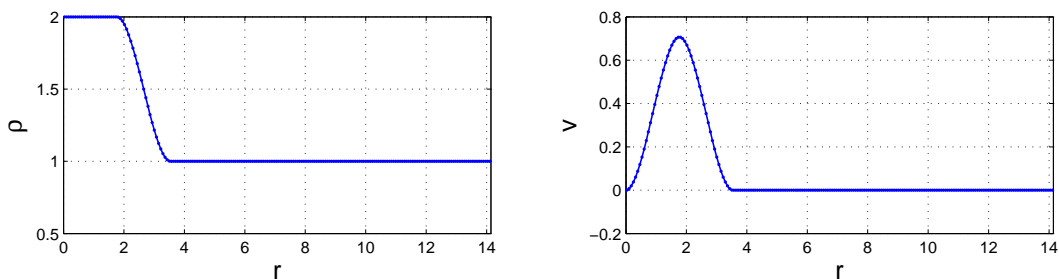


Figure 1: Piecewise polynomial  $C^1$  initial data for the relativistic Euler equations along the radial direction. Left panel: density; Right panel: velocity.

Fig. 2 illustrates the profiles of  $\rho$  and  $v$  at time  $t = 5.75$  with 200 grid cells on the domain  $[0, 10\sqrt{2}]$ . The three results agree well in the smooth regions and the positions of the discontinuities are approximately matched. The hybrid method produces a sharp discontinuity: the zoom plots in the right panels illustrate that there is “no point in the discontinuity” when using the hybrid method, while there are three or four points in this area for the central-upwind scheme in both one and two-dimensions.

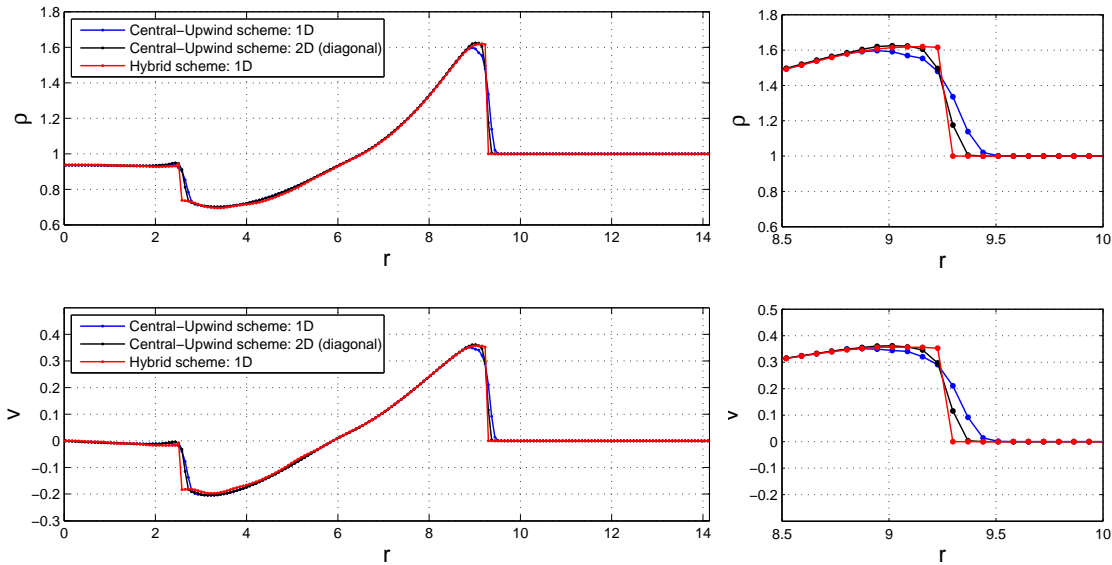


Figure 2: Numerical solutions of the relativistic Euler equations at time  $t=5.75$  with  $\beta=0.7$  and  $M=1.0$ . The radial case is solved with 200 grid cells of size  $\Delta r=0.05\sqrt{2}$ . The two-dimensional scheme uses a Cartesian grid of size  $\Delta x=\Delta y=0.05$ . Top panels: density; Bottom panels: velocity; Right panels: zoom around the discontinuity area.

## 4 Shock formation

Further analysis is required to assess the precise nature of apparent discontinuities such as those from Fig. 2. As mentioned in the Introduction, numerically checking whether the Rankine-Hugoniot conditions hold is highly impractical. Since both the instantaneous speed and the jump height of the discontinuity are varying as the discontinuity propagates, it is difficult to accurately compute the speed of the discontinuity from the solution and obtain the values immediately to the left and right of the discontinuity. Therefore, we propose a numerical approach based on direct characteristic analysis. We first use a classical example as an illustration.

### 4.1 A classical example: Sod shock tube problem of Euler equations

This well-known test is a one-dimensional Riemann problem for a polytropic gas [34]. The following left and right states are considered

$$\begin{pmatrix} \rho_L \\ p_L \\ v_L \end{pmatrix} = \begin{pmatrix} 1.0 \\ 1.0 \\ 0.0 \end{pmatrix}, \quad \begin{pmatrix} \rho_R \\ p_R \\ v_R \end{pmatrix} = \begin{pmatrix} 0.125 \\ 0.1 \\ 0.0 \end{pmatrix}.$$

As shown in Fig. 3, the solution consists of a shock moving into the gas at lower pressure and a rarefaction wave that expands into the gas at higher pressure. In between there is

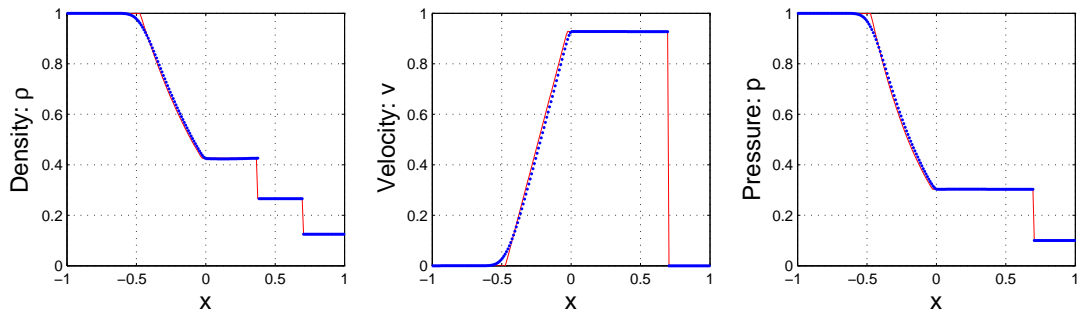


Figure 3: Numerical solutions of the Sod shock tube problem of the one-dimensional Euler equations for polytropic gas. We solve the system with 200 grid cells of size  $\Delta x = 0.01$ . The blue dots represent the result obtained by using the hybrid method. The red line represents the exact solution. Left panel: density; middle panel: velocity; right panel: pressure.

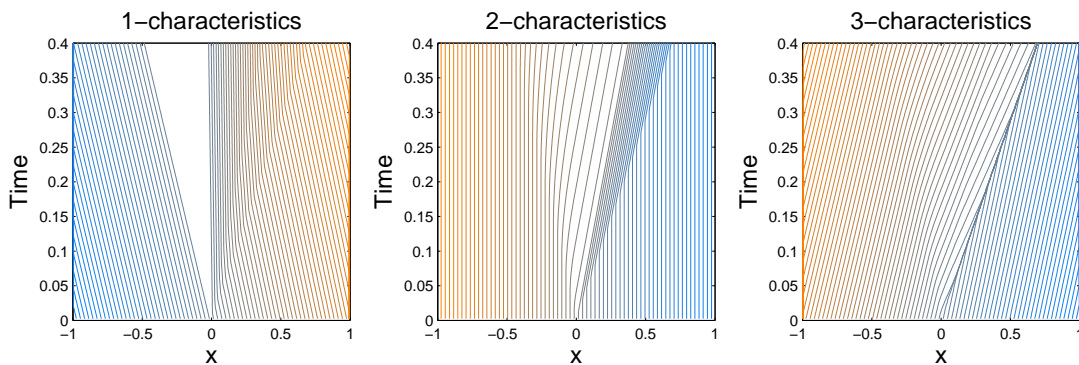


Figure 4: The characteristics fields of the Sod shock tube problem. From left to right panels are 1-, 2-, 3-characteristics, respectively. See the text for details.

a contact discontinuity, across which the velocity  $v$  and pressure  $p$  are constant and the density  $\rho$  jumps.

There are three characteristics that describe the propagation speeds of the various regions of the system. They are given by the eigenvalues of the Jacobian matrix of the system, i.e.,  $\lambda_1 = v - s$ ,  $\lambda_2 = v$ ,  $\lambda_3 = v + s$ , where  $s$  is the sound speed, see [23] for details. Fig. 4 shows the characteristics fields in the  $x-t$  plane. In the left panel of 1-characteristics field, there is a blank region where the rarefaction wave lies. The middle panel shows that the 2-characteristics on both sides of the contact discontinuity run parallel to it. In the right panel, the 3-characteristics on each side of the shock run into the shock as time advances.

#### 4.2 The characteristics of the relativistic Euler equations

The system (2.10)-(2.11) can be rewritten in the following quasi-linear form

$$U_t + \mathbf{A}(U)U_x = \mathbf{G}(U), \tag{4.1}$$

where the Jacobian matrix  $\mathbf{A}(\mathbf{U})$  is given by

$$\mathbf{A}(\mathbf{U}) = \left( \frac{\partial \mathbf{W}}{\partial \mathbf{U}} \right)^{-1} \frac{\partial \mathbf{F}}{\partial \mathbf{U}} \quad (4.2)$$

with

$$\mathbf{U} = \begin{pmatrix} \rho \\ v_r \end{pmatrix}, \quad \mathbf{W} = \begin{pmatrix} \hat{\rho} \\ \tilde{\rho} v_r \end{pmatrix}, \quad \mathbf{F} = \begin{pmatrix} \tilde{\rho} v_r \\ \tilde{\rho} v_r^2 + \frac{1}{\gamma M^2} \rho^\gamma \end{pmatrix},$$

and where  $\mathbf{G}(\mathbf{U})$  represents the geometrical source terms. Straightforward calculations yield

$$\frac{\partial \mathbf{W}}{\partial \mathbf{U}} = \begin{pmatrix} \frac{\partial \tilde{\rho}}{\partial \rho} - \frac{\beta^2 \rho^{\gamma-1}}{M^2} & \frac{\partial \tilde{\rho}}{\partial v_r} \\ \frac{\partial \tilde{\rho}}{\partial \rho} v_r & \frac{\partial \tilde{\rho}}{\partial v_r} v_r + \tilde{\rho} \end{pmatrix}, \quad \frac{\partial \mathbf{F}}{\partial \mathbf{U}} = \begin{pmatrix} \frac{\partial \tilde{\rho}}{\partial \rho} v_r & \frac{\partial \tilde{\rho}}{\partial v_r} v_r + \tilde{\rho} \\ \frac{\partial \tilde{\rho}}{\partial \rho} v_r^2 + \frac{\rho^{\gamma-1}}{M^2} & \frac{\partial \tilde{\rho}}{\partial v_r} v_r^2 + 2\tilde{\rho} v_r \end{pmatrix},$$

with the partial derivatives

$$\frac{\partial \tilde{\rho}}{\partial \rho} = \frac{1 + \frac{\beta^2}{M^2} \rho^{\gamma-1}}{1 - \beta^2 v_r^2}, \quad \frac{\partial \tilde{\rho}}{\partial v_r} = \tilde{\rho} \frac{2\beta^2 v_r}{1 - \beta^2 v_r^2}.$$

The characteristics speeds of the system are then given by the eigenvalues of  $\mathbf{A}(\mathbf{U})$  in (4.2). We numerically compute the eigenvalues to track the characteristics.

### 4.3 Numerical results

We start by solving (2.10)-(2.11) up to time  $t = 8.0$  with 320 grid cells on the domain  $[0, 10\sqrt{2}]$ . The initial conditions are those of Fig. 1. Fig. 5 illustrates results from the hybrid method for  $\beta = 0.2$  and  $M = 1.0$ . The top panels show the profiles of density and velocity at different times. The bottom panels show the 1- and 2-characteristics, which are corresponding to the small and large eigenvalues of the linearized matrix  $\mathbf{A}(\mathbf{U})$  in (4.2). We track each characteristic curve starting from each of the grid points that are equally spaced on the domain  $[0, 10\sqrt{2}]$ . In Figs. 5 and 6, for clarity we only show characteristic curves starting from every four grid points. Therefore, there are total 80 curves starting from the bottom of the domain. Some 2-characteristics on each side of the discontinuity run into it, indicating a shock.

Fig. 6 illustrates the same experiment but with  $\beta = 0.7$ . A casual look at the characteristics does not bring as definite an answer as the previous case. This is due to the presence of small plateaus to the left of the discontinuity.

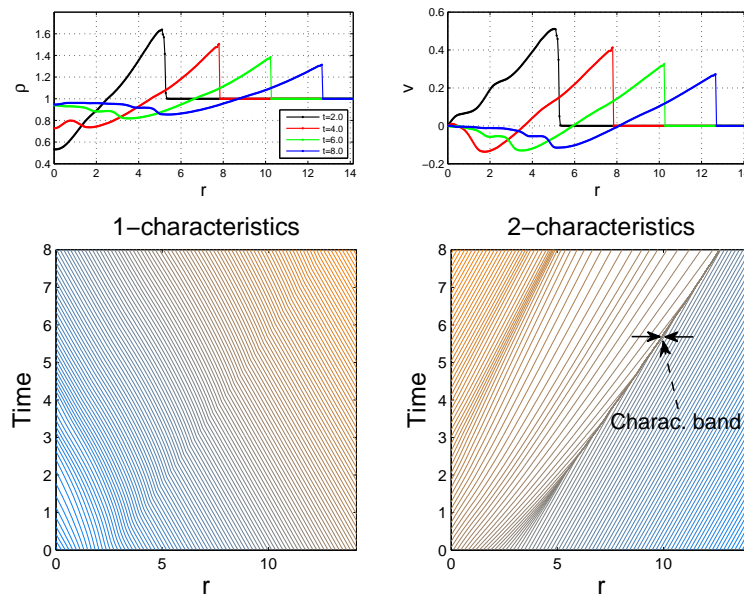


Figure 5: Top panels: numerical solutions of the relativistic Euler equations at different times  $t = 2.0, 4.0, 6.0,$  and  $8.0,$  with the parameters  $\beta = 0.2$  and  $M = 1.0,$  (top left): density, (top right): velocity. We solve the radial system with 320 grid cells along the radial direction, i.e.,  $\Delta r = 0.03125\sqrt{2}.$  Bottom panels: 1- and 2-characteristics.

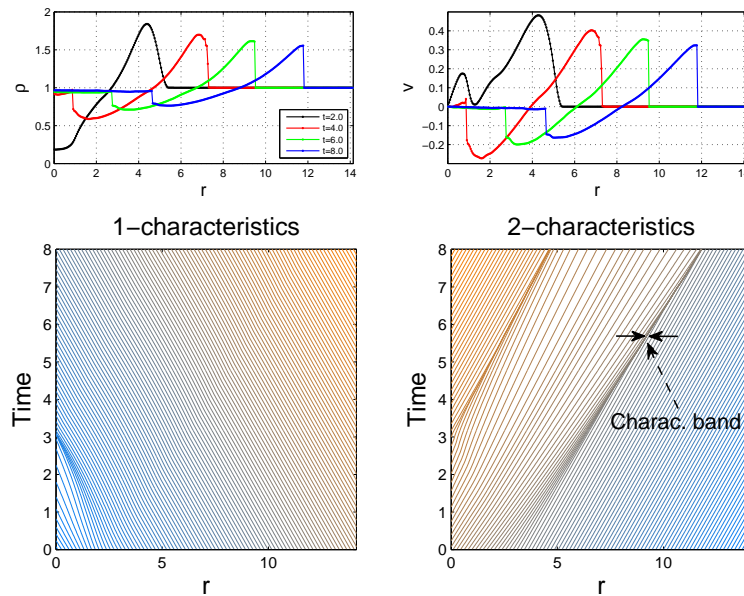


Figure 6: Top panels: numerical solutions of the relativistic Euler equations at different times  $t = 2.0, 4.0, 6.0,$  and  $8.0,$  with the parameters  $\beta = 0.7$  and  $M = 1.0,$  (top left): density, (top right): velocity. We solve the radial system with 320 grid cells along the radial direction, i.e.,  $\Delta r = 0.03125\sqrt{2}.$  Bottom panels: 1- and 2-characteristics.

To better numerically analyze the nature of possible discontinuities, we introduce a notion of “characteristic band”. The corresponding numerical post-processing is as follows. First, we generate, on the boundary of the computational domain, a set of starting points for the characteristic curves. The slope fields for the characteristic curves are defined by

$$\frac{dr_{i,j}(t)}{dt} = \lambda_i(r_{i,j}(t), t), \quad i=1,2, \quad (4.3)$$

where the  $\lambda_i$ 's are the eigenvalues of  $\mathbf{A}(\mathbf{U})$  in (4.2) and where the indices  $i$  and  $j$  refer respectively to the characteristic family and to the starting point. In this post-processing step, the Jacobian is available at every spatial node and at discrete times. For the purpose of the calculations in (4.3),  $\mathbf{A}(\mathbf{U})$  is taken piecewise constant in time and is linearly interpolated in space. Eqs. (4.3) are solved through a simple forward Euler scheme.

An  $\epsilon$ -band at time  $t$  for the  $i$ -th characteristic field is defined as

$$\mathcal{B}_i(t) = \bigcup_{j=\ell_{\min}}^{\ell_{\max}} r_{i,j}(t), \quad \text{where } |r_{i,j+1}(t) - r_{i,j}(t)| < \epsilon \quad \forall j = \ell_{\min}, \dots, \ell_{\max} - 1, \quad (4.4)$$

with  $|r_{i,\ell_{\max}+1}(t) - r_{i,\ell_{\max}}(t)| \geq \epsilon$  and  $|r_{i,\ell_{\min}}(t) - r_{i,\ell_{\min}-1}(t)| \geq \epsilon$ . The width  $w_i(t)$  and the number of curves  $n_i(t)$  of  $\mathcal{B}_i(t)$  are given by

$$w_i(t) = |r_{i,\ell_{\max}}(t) - r_{i,\ell_{\min}}(t)| \quad \text{and} \quad n_i(t) = \ell_{\max} - \ell_{\min} + 1.$$

Our analysis will conclude the likely presence of a shock if, over a certain time interval,  $w_i$  is non-increasing and  $n_i$  is non-decreasing. Both of the cases in Figs. 5 and 6 correspond to shocks when the above criterion is applied. Here and below, we use  $\epsilon = \Delta r / 2$ .

We can now proceed to a systematic scanning in parameter space. We choose two sets of equally spaced values of  $M = 0.25, 0.5, \dots, 2.0$  and the ratio  $\frac{\beta}{M} = 0.05, 0.1, \dots, 0.7$ , due to condition (2.12) requiring that  $\frac{\beta}{M} < 1/\sqrt{2} \approx 0.707$ . For each pair of values of  $\beta$  and  $M$ , we use the hybrid method to solve the radial system (2.10)-(2.11) with 320 grid cells on the domain  $[0, 10\sqrt{2}]$  up to a certain time when the wave front (discontinuity) in the density profile arrives at a fixed location  $r = 10$ . The initial conditions are again taken from Section 3.

Fig. 7 shows the scanning result of the estimated width of the characteristics band around  $r = 10$  for the above values of the parameters  $\beta$  and  $M$ . Region A corresponds to the part of parameter space in which singularity formation has been established [29]. Our numerical results are consistent with this analysis and in fact, according to the above criterion, predict shock formation. The same is true for the entire lower “plateau” in Fig. 7. While the solutions corresponding the parameter choices in the upper-left corner in Fig. 7 may appear to be different, it turns out that if the wave is given enough time to develop by extending the computational domain, even these cases lead to shock formation. This process is explicitly illustrated in Fig. 8 where the width of the characteristic band and

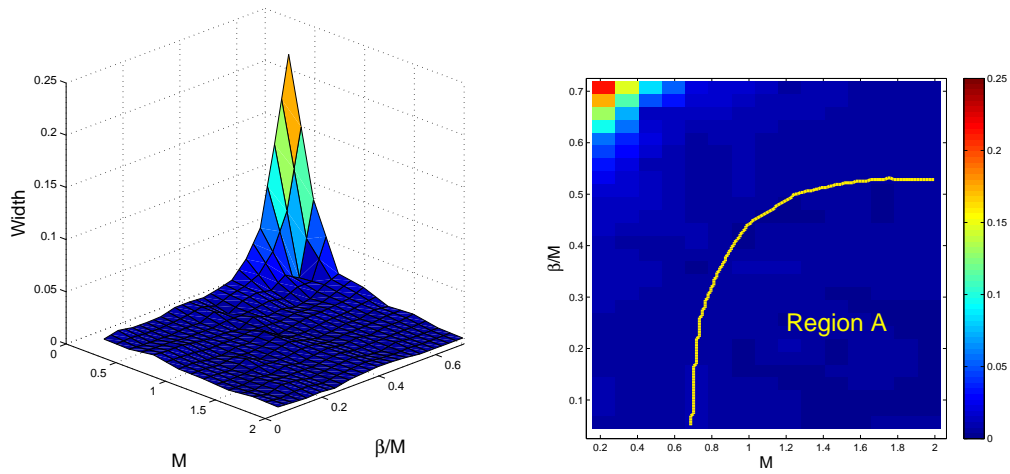


Figure 7: Scanning result of the estimated width of the characteristic band around  $r=10$  for (2.10)-(2.11) with  $d=2$ . Right panel: in the region A under the yellow dashed curve, the initial condition (2.15) for finite time singularity formation is satisfied.

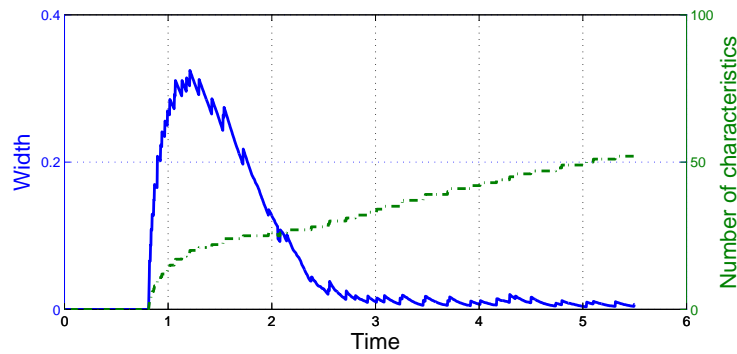


Figure 8: Evolution of the width (solid line, left axis) of the  $\epsilon$ -characteristic band and of the number of contained curves (dashed line, right axis) for (2.10)-(2.11) with  $d=2$ , 320 grid cells,  $\epsilon = \Delta r/2$  with  $M=0.25$  and  $\beta=0.7$  from  $t=0$  to  $t=5.5$ . The zigzag profile is due to the integer numbers of the characteristics counted in the band.

the number of characteristic curves in it are displayed as a function of time (for  $M=0.25$  and  $\frac{\beta}{M}=0.7$ ).

It is interesting to extend this study to the spherically symmetric case (2.10)-(2.11) with  $d=3$ , i.e., in (3+1)-dimensional spacetime. Even though one might expect the source terms to play here a bigger role, we obtain very similar results. We have also performed a systematic scanning test for two sets of equally spaced values of  $M=0.25, 0.5, \dots, 2.0$  and the ratio  $\frac{\beta}{M}=0.04, 0.08, \dots, 0.56$ , since condition (2.16) requires that  $\frac{\beta}{M} < 1/\sqrt{3} \approx 0.577$ . The results are displayed in Fig. 9 and correspond again to shock formation. Finally, we obtain qualitatively identical results for values of the adiabatic index  $\gamma$  between 1 and 2 (1.1, 1.2,  $\dots$ , 2.0) and thus our singularity formation analysis is independent of that choice.

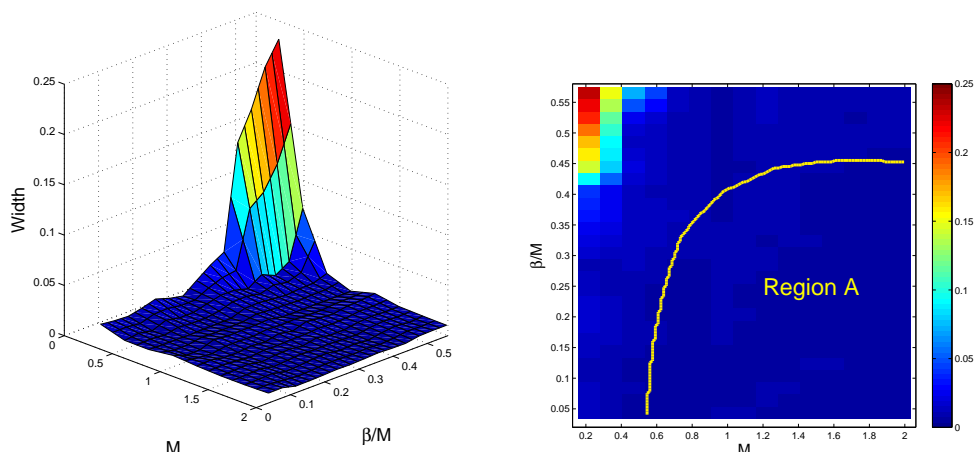


Figure 9: Scanning result of the estimated width of the characteristic band around  $r=10$  for (2.10)-(2.11) with  $d=3$ . Right panel: in the region A under the yellow dashed curve, the initial condition (2.17) for finite time singularity formation is satisfied.

## 5 Conclusions

We have proposed a new method for the analysis of singularity formation in hyperbolic balance laws. The method is based on a hybrid Glimm-finite difference discretization and on a local numerical analysis of the characteristic curves.

While it is expected that our approach can be widely applied, we concentrate here on the relativistic Euler equations for perfect fluids. This new tool allows us to contribute to the answer of an open theoretical question, namely: which mechanism leads to singularity formation for these equations? For a specific family of problems and initial conditions, shock formation is found to occur rather than violation of the subluminal condition or mass concentration. Further studies involving different initial conditions may discover that the other two mechanisms could also be realized. We emphasize that since the extension of Glimm's method to generic two or three dimensional systems is still an open issue, our method is ideal for the system with radial symmetry in two dimensional or with spherical symmetry in three dimensional. Detecting shocks in two or three dimensional systems without symmetries is more challenging.

## Appendix

The Glimm scheme was introduced in [13] and developed into a numerical method for hyperbolic conservation laws in [5]. As is well known, it consists of two steps: (1) the solution is approximated at each time step by piecewise constant states, and local Riemann problems formed by the neighboring states are solved; (2) the solution at the next time step is taken to be the exact solution of these Riemann problems at a randomly chosen point inside each mesh cell.

The solution to the Riemann problem in Newtonian hydrodynamics was derived by Godunov [14]. For relativistic hydrodynamics, Smoller and Temple [33] constructed the analytic solution to the Riemann problem in the isothermal case  $p(\rho) = \sigma^2 \rho$ , i.e.,  $\gamma = 1$  in the  $\gamma$ -law. For  $\gamma > 1$ , we need to obtain the solution numerically.

The first step is to determine the intermediate state  $(\rho_M, v_M)$  given left and right states  $(\rho_K, v_K)$ ,  $K=L, R$ . This can be done by using the Rankine-Hugoniot relations across shocks and the Riemann invariants across rarefaction waves. From the Rankine-Hugoniot relations across shocks, we obtain a first equation:

$$\rho^{\gamma+1} - C_1 \rho^\gamma - C_2 \rho + \rho_K^{\gamma+1} = 0, \quad K=L, R, \tag{A.1}$$

with

$$C_1 \equiv C_1(v, \rho_K, v_K) = \frac{(1 - \beta^2 v v_K)^2 \rho_K + \frac{\beta^4}{\gamma M^2} (v - v_K)^2 \rho_K^\gamma}{(1 - \beta^2 v^2)(1 - \beta^2 v_K^2)},$$

$$C_2 \equiv C_2(v, \rho_K, v_K) = \frac{(1 - \beta^2 v v_K)^2 \rho_K^\gamma + \gamma M^2 (v - v_K)^2 \rho_K}{(1 - \beta^2 v^2)(1 - \beta^2 v_K^2)}.$$

Following Section 4 of [33], 1-shocks are parametrized by  $\rho \geq \rho_K$  and 2-shocks by  $\rho \leq \rho_K$ , the distinction between the two being made by referring to the eigenvalues of (4.2). A second equation is derived from the Riemann invariants, i.e.,

$$I_{1,2}(\rho, v) = \frac{1}{2} \ln \left( \frac{1 + \beta v}{1 - \beta v} \right) \pm \frac{2\sqrt{\gamma}}{\gamma - 1} \arctan \left( \frac{\beta}{\sqrt{\gamma} M} \rho^{\frac{\gamma-1}{2}} \right). \tag{A.2}$$

While the process can be graphically illustrated in Fig. 10, its practical implementation relies on [37].

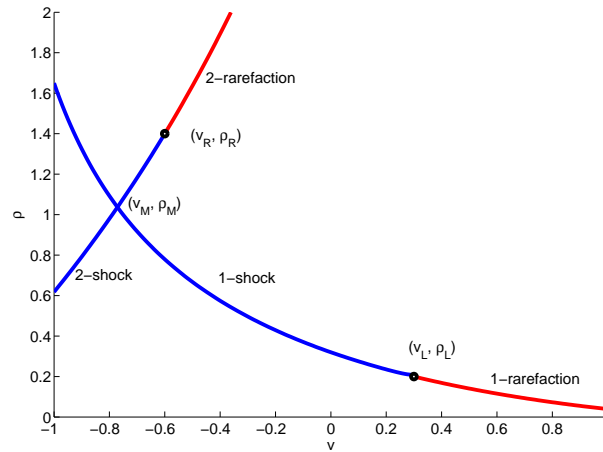


Figure 10: Illustration of the Hugoniot loci and rarefaction curves for two specific left and right states  $(\rho_K, v_K)$ ,  $K=L, R$ .

The second step in solving a Riemann problem is to completely determine the left and right waves. For shock waves, we only need to find the shock speed. For rarefaction waves, the head and tail of the wave and the full solution inside the rarefaction fan have to be determined.

With the Riemann solver in hand, the Glimm scheme updates the solution  $U = (\rho, v)$  from  $U_i^n$  in  $i$ -th cell at time level  $n$ , to the value  $U_i^{n+1}$  at time level  $n+1$  as follows. First, we solve the Riemann problems  $RP(U_{i-1}^n, U_i^n)$  and  $RP(U_i^n, U_{i+1}^n)$  to find their respective solutions  $U_{i-\frac{1}{2}}(\frac{x}{t})$  and  $U_{i+\frac{1}{2}}(\frac{x}{t})$ . Then we randomly sample these solutions at time  $\Delta t$  within  $i$ -th cell to pick up a state and assign it to  $i$ -th cell. The choice depends on a random number  $\zeta^n$  in the interval  $[0,1]$ . The updated solution is given by

$$U_i^{n+1} = \begin{cases} U_{i-\frac{1}{2}}(\zeta^n \frac{\Delta x}{\Delta t}), & \text{if } 0 \leq \zeta^n \leq \frac{1}{2}, \\ U_{i+\frac{1}{2}}((\zeta^n - 1) \frac{\Delta x}{\Delta t}), & \text{if } \frac{1}{2} \leq \zeta^n \leq 1. \end{cases}$$

Details about appropriate random number generators can be found in Colella [6].

## Acknowledgments

We would like to thank Joel Smoller, Randy LeVeque and Jian-Guo Liu for useful discussions and the reviewers for their helpful comments to improve this paper. P. Gremaud's research is partially supported by the National Science Foundation (NSF) through grants DMS-0811150. Y. Sun's research is partially supported by NSF through the NSF Joint Institutes' Postdoctoral Fellowship at SAMSI and a USC startup fund.

## References

- [1] A. M. Anile, *Relativistic Fluids and Magnetofluids*, Cambridge University Press, London, 1989.
- [2] P. Anninos and P. Fragile, Nonoscillatory central difference and artificial viscosity schemes for relativistic hydrodynamics, *Astrophys. J. Suppl. Ser.*, 144 (2003), 243-257.
- [3] C. Bona, C. Palenzuela-Luque, and C. Bona-Casas, *Elements of Numerical Relativity and Relativistic Hydrodynamics: From Einstein's Equations to Astrophysical Simulations*, 2nd ed., *Lect. Notes in Phys.* 783, Springer, Berlin, 2009.
- [4] J. K. Cannizzo, N. Gehrels and E. T. Vishniac, Glimm's method for relativistic hydrodynamics, *Astrophys. J.*, 680 (2008), 885-896.
- [5] A. J. Chorin, Random choice solution of hyperbolic systems, *J. Comput. Phys.*, 22 (1976), 517-533.
- [6] P. Colella, Glimm's method for gas dynamics, *SIAM J. Sci. Stat. Comput.*, 3 (1982), 76-110.
- [7] P. Colella and P. Woodward, The piecewise-parabolic method (PPM) for gas-dynamical simulations, *J. Comput. Phys.*, 54 (1984), 174-201.
- [8] L. Del Zanna and N. Bucciantini, An efficient shock-capturing central-type scheme for multi-dimensional relativistic flows. I. Hydrodynamics, *Astron. Astrophys.*, 390 (2002), 1177-1186.
- [9] A. Dolezal and S. S. M. Wong, Relativistic hydrodynamics and essentially non-oscillatory shock capturing schemes, *J. Comput. Phys.*, 120 (1995), 266-277.

- [10] B. Einfeldt, On Godunov-type methods for gas dynamics, *SIAM J. Numer. Anal.*, 25 (1988), 294-318.
- [11] F. Eulderink and G. Mellema, General relativistic hydrodynamics with a Roe solver, *Astron. Astrophys. Suppl.*, 110 (1995), 587-623.
- [12] J. A. Font, Numerical hydrodynamics and magnetohydrodynamics in general relativity, *Living Rev. Relativity*, 11 (2008), <http://relativity.livingreviews.org/Articles/lrr-2008-7>
- [13] J. Glimm, Solutions in the large for nonlinear hyperbolic systems of equations, *Commun. Pure Appl. Math.*, 18 (1965), 697-715.
- [14] S. K. Godunov, A finite difference method for the numerical computation of discontinuous solutions of the equations of fluid dynamics, *Mat. Sb.*, 47 (1959), 271-290.
- [15] A. Harten, P. D. Lax, and B. van Leer, On upstream differencing and Godunov-type schemes for hyperbolic conservation laws, *SIAM Rev.*, 25 (1983), 35-61.
- [16] P. He, H. Z. Tang, An adaptive moving mesh method for two-dimensional relativistic hydrodynamics, *Commun. Comput. Phys.*, 11 (2012), 114-146.
- [17] J. Hu and S. Jin, On the quasi-random choice method for Liouville equation of geometrical optics with discontinuous wave speed, *J. Comput. Math*, 31 (2013), 573-591.
- [18] A. Kurganov, S. Noelle, and G. Petrova, Semidiscrete central-upwind schemes for hyperbolic conservation laws and Hamilton-Jacobi equations, *SIAM J. Sci. Comput.*, 23 (2001), 707-740.
- [19] A. Kurganov and E. Tadmor, New high resolution central schemes for nonlinear conservation laws and convection-diffusion equations, *J. Comput. Phys.*, 160 (2000), 241-282.
- [20] A. Kurganov and E. Tadmor, Solution of two-dimensional Riemann problems for gas-dynamics without Riemann problem solvers, *Numer. Methods Partial Differential Equations*, 18 (2002), 584-608.
- [21] P. Lax, Development of singularity of solutions of nonlinear hyperbolic partial differential equations, *J. Math. Phys.*, 5 (1964), 611-613.
- [22] P.G. LeFloch and M. Yamazaki, Entropy solutions of the Euler equations for isothermal relativistic fluids, *Int. J. Dynamical Systems and Differential Equations*, 1 (2007), 20-37.
- [23] R.J. LeVeque, *Finite Volume Methods for Hyperbolic Problems*, Cambridge University Press, Cambridge, 2002.
- [24] A. Lucas-Serrano, J. A. Font, J. M. Ibáñez, and J. M. Martí, Assessment of a high-resolution central scheme for the solution of the relativistic hydrodynamic equations, *Astron. Astrophys.*, 428 (2004), 703-715.
- [25] J. M. Martí and E. Müller, The analytical solution of the Riemann problem in relativistic hydrodynamics, *J. Fluid Mech.*, 258 (1994), 317-333.
- [26] J. M. Martí and E. Müller, Extension of the piecewise parabolic method to one-dimensional relativistic hydrodynamics, *J. Comput. Phys.*, 123 (1996), 1-14.
- [27] J. M. Martí and E. Müller, Numerical hydrodynamics in special relativity, *Living Rev. Relativity*, 6 (2003), <http://relativity.livingreviews.org/Articles/lrr-2003-7>
- [28] F. Miniati, Glimm-Godunov's method for cosmic-ray-hydrodynamics, *J. Comput. Phys.*, 227 (2007), 776-796.
- [29] R. Pan and J.A. Smoller, Blowup of smooth solutions for relativistic Euler equations, *Commun. Math. Phys.*, 262 (2006), 729-755.
- [30] P. L. Roe, Approximate Riemann solvers, parameter vectors and difference schemes, *J. Comput. Phys.*, 43 (1981), 357-372.
- [31] V. Schneider, V. Katscher, D. H. Rischke, B. Waldhauser, J. A. Marhun, and C.-D. Munz, New algorithms for ultra-relativistic numerical hydrodynamics, *J. Comput. Phys.*, 105 (1993), 92-

107.

- [32] J. Smoller, *Shock Waves and Reaction-Diffusion Equations*, 2nd ed., Grundlehren Math. Wiss. 258, Springer-Verlag, New York, 1994.
- [33] J. Smoller and B. Temple, Global solutions of the relativistic Euler equations, *Commun. Math. Phys.*, 156 (1993), 67-99.
- [34] G. Sod, A survey of several finite difference methods for systems of nonlinear hyperbolic conservation laws, *J. Comput. Phys.*, 22 (1978), 1-31.
- [35] A. H. Taub, Relativistic fluid mechanics, *Annu. Rev. Fluid Mech.*, 10 (1978), 301-332.
- [36] K. Thompson, The special relativistic shock tube. *J. Fluid Mech.*, 171 (1986), 365-375.
- [37] E. Toro, *Riemann Solvers and Numerical Methods for Fluid Dynamics*, Springer, Berlin, 1999.
- [38] R. M. Wald, ed. *Black holes and Relativistic Stars*, University of Chicago Press, Chicago, 1998.
- [39] L. Wen, A. Panaitescu, and P. Laguna, A shock-patching code for ultrarelativistic fluid flows, *Astrophys. J.*, 486 (1997), 919-927.
- [40] J. R. Wilson and G. J. Mathews, *Relativistic numerical hydrodynamics*, Cambridge University Press, Cambridge, 2003.
- [41] J. Y. Yang, M. H. Chen, I. N. Tsai, and J. W. Chang, A kinetic beam scheme for relativistic gas dynamics, *J. Comput. Phys.*, 136 (1997), 19-40.
- [42] Z. C. Yang, P. He, H. Z. Tang, A direct Eulerian GRP scheme for relativistic hydrodynamics: one-dimensional case, *J. Comput. Phys.*, 230 (2011), 7964-7987.
- [43] Z. C. Yang and H. Z. Tang, A direct Eulerian GRP scheme for relativistic hydrodynamics: two-dimensional case, *J. Comput. Phys.*, 231 (2012), 2116-2139.
- [44] W. Q. Zhang and A. I. MacFadyen, RAM: a relativistic adaptive mesh refinement hydrodynamics code, *Astrophys. J. Suppl.*, 164 (2006), 255-279.
- [45] J. Zhao and H. Z. Tang, RungeKutta discontinuous Galerkin methods with WENO limiter for the special relativistic hydrodynamics, *J. Comput. Phys.*, 242 (2013), 138-168.
- [46] Y.H. Zahran, RCM-TVD hybrid scheme for hyperbolic conservation laws, *Int. J. Numer. Meth. Fluids*, 57 (2007), 745-760.